



Published in final edited form as:

*Magn Reson Med.* 2010 August ; 64(2): 491–500. doi:10.1002/mrm.22440.

## Optimized Inversion Recovery Sequences for Quantitative $T_1$ and Magnetization Transfer Imaging

Ke Li<sup>1,2</sup>, Zhongliang Zu<sup>1,2</sup>, Junzhong Xu<sup>1,2</sup>, Vaibhav A. Janve<sup>1,3</sup>, John C. Gore<sup>1,2,4</sup>, Mark D. Does<sup>1,2,4</sup>, and Daniel F. Gochberg<sup>1,2,3</sup>

<sup>1</sup>Vanderbilt University Institute of Imaging Science, Vanderbilt University, Nashville, Tennessee, USA

<sup>2</sup>Department of Radiology and Radiological Sciences, Vanderbilt University, Nashville, Tennessee, USA

<sup>3</sup>Department of Physics and Astronomy, Vanderbilt University, Nashville, Tennessee, USA

<sup>4</sup>Department of Biomedical Engineering, Vanderbilt University, Nashville, Tennessee, USA

### Abstract

Inversion recovery sequences that vary the inversion time ( $t_i$ ) have been employed to determine  $T_1$  and, more recently, quantitative magnetization transfer (qMT) parameters. Specifically, in previous work, the inversion recovery pulse sequences varied  $t_i$  only, while maintaining a constant delay ( $t_d$ ) between repetitions.  $T_1$  values were determined by fitting to an exponential function, and qMT parameters were then determined by fitting to a bi-exponential function with an approximate solution. In the current study, new protocols are employed, which vary both  $t_i$  and  $t_d$  and fit the data with minimal approximations. Cramer-Rao lower bounds (CRLB) are calculated to search for acquisition schemes that will maximize the precision efficiencies of  $T_1$  and qMT parameters. This approach is supported by Monte Carlo simulations. Measurements on  $\text{MnCl}_2$  samples verified the optimal  $T_1$  schemes. The optimal qMT schemes are confirmed by measurements on a series of cross linked bovine serum albumin (BSA) phantoms of varying concentrations. The effects of varying the number of sampling data points are also explored, and a rapid acquisition scheme is demonstrated *in vivo*. These new optimized quantitative imaging methods provide an improved means for determining  $T_1$  and MT parameter values compared to previous inversion recovery based methods.

### Keywords

Quantitative magnetization transfer;  $T_1$  measurement; Inversion recovery; Bi-exponential recovery; Optimal acquisition scheme; Precision efficiency

### Introduction

Magnetization Transfer (MT), or spin exchange between protons in different tissue pools, can serve as a contrast mechanism in biological systems. MT between free water and a broad, immobile pool of protons on macromolecules, was first demonstrated by Wolff and Balaban (1), who measured the equilibrium magnetization ( $M_s$ ) of water protons after applying continuous irradiation. Subsequently, Henkelman *et al.* (2) developed a two-pool

model and performed measurements on agar gels. By varying the RF offset frequency and amplitude; they determined the relaxation and exchange rates of the two proton pools. This determination of the underlying sample parameters is referred to as quantitative magnetization transfer (qMT).

Several qMT imaging methods have been developed. Sled and Pike (3,4) extended the technique of Henkelman *et al.* to pulsed-MT, in which off-resonance saturation pulses are interleaved with on-resonance excitation pulses. Ramani *et al.* (5) combined the method of Sled and Pike with an analysis similar to Henkelman *et al.* Gloor *et al.* (6) developed a qMT imaging method based on balanced steady state free precession (SSFP), while Ropele *et al.* (7) developed a method based on stimulated echoes. Gochberg *et al.* (8-10) developed a selective-inversion-recovery (SIR) technique, a qMT imaging method based on measuring the transient response to an RF pulse that selectively inverts the free water protons. MT induces bi-exponential recovery of longitudinal magnetization in most tissue types, including *in vitro* collagen (11,12), muscle (11), cartilage (13) and lung (14), and *in vivo* white matter (WM), grey matter (GM) and muscle (10). Prantner *et al.* (15) examined and dismissed non-MT explanations for this bi-exponential in brain matter. In the most recent version of the SIR method (10), a fast-spin-echo (FSE) readout is applied, which leaves both the liquid and solid proton pools saturated and therefore facilitates determination of qMT parameters using shorter repetition times.

The precision and accuracy of the estimates of the qMT parameters depend on several experimental factors, such as the MT pulse power ( $\omega_1$ ) and offset frequency ( $\Delta$ ) for pulsed-MT, and the inversion recovery time ( $t_i$ ) and pre-delay time ( $t_d$ ) values for SIR-FSE. In most published MT protocols, the set of sampling points is selected empirically. Cramer-Rao lower bounds (CRLB) (16) provide a general approach to assess this dependence on acquisition parameters, by setting a lower limit on the variance of any parameter estimate based on model fitting. This method has been used to optimize acquisition schemes for  $T_1$  measurements with constrained scan time (17),  $T_2$  measurements (18), diffusion coefficients (19), and echo spacing for multi-echo imaging (20). In Sled and Pike's pulsed-MT work (4), they used only two values of  $\omega_1$ , each with a range of  $\Delta$ . Based on Ramani's model (5), the pulsed-MT technique was optimized by Cercignani *et al.* (21) by calculating the CRLB to obtain optimal acquisition protocols.

For the SIR-FSE technique (10), Gochberg *et al.* used a constant  $t_d$  and varied  $t_i$  only. The experimental data were then fitted to a bi-exponential equation to determine first-order approximations of the qMT parameters. The current paper focuses on the optimization of this technique (10), introduces a new data analysis method as part of this optimization, and employs a new protocol that varies both  $t_i$  and  $t_d$  and fits the data with minimal approximations. CRLB are calculated to search for the variations in both  $t_i$  and  $t_d$  that will maximize the precision efficiency. The optimal schemes are supported by Monte Carlo simulations, and confirmed by measurements on BSA phantoms. It is further demonstrated that, in practice, only five sampling points are required to determine qMT parameters and is confirmed with *in vivo* rat brain measurements.

SIR-FSE is essentially an inversion recovery (IR) method with the assumption of bi-exponential recovery due to MT. Independently varying  $t_i$  and  $t_d$  also improves the precision efficiency of simple  $T_1$  measurements, when assuming a single exponential recovery. While this method is often replaced by the more rapid single shot (22,23) and variable-flip-angle (VFA) methods (24-26), we include a variable  $t_i$  and  $t_d$  analysis of  $T_1$  here for its inherent interest and as an introduction to the more complex qMT case.

## Theory and Methods

### IR Imaging Sequence

Conventionally,  $T_I$  is determined by using an IR sequence (similar to Figure 1) with  $t_d \geq 5 T_I$ , during which the magnetization returns to its equilibrium state before the next sequence repetition. Previous work has optimized  $T_I$  measurement efficiency using constant  $t_d$  or constant repetition time (TR) (17). Here we will take a more general approach, by varying both  $t_i$  and  $t_d$  independently without constraint. For an IR with a spin-echo (SE) or fast-spin-echo (FSE) readout, the measured signal is:

$$S = M_0 \left[ S_f \left( 1 - e^{-t_d/T_1} \right) e^{-t_i/T_1} + 1 - e^{-t_i/T_1} \right] \quad [1]$$

where  $M_0$  is the magnetization of the equilibrium state, and  $S_f (\approx -1)$  quantifies the effect of the inversion pulse.

### SIR-FSE qMT Imaging Sequence

The SIR-FSE pulse sequence (10) is illustrated in Figure 1. In order to model the signal when TR is short, an essential insight is that at the end of each repetition, both the macromolecular and free water pools have zero  $z$ -magnetization. The assumption has been discussed numerically and verified previously (10).

The qMT data analysis is based on a two-pool model. The coupling between the pools is modeled by adding coupling terms to the Bloch equations, as given in (9,10):

$$\begin{aligned} \frac{d}{dt} \frac{M_f(t)}{M_{f\infty}} &= -R_{1f} \left( \frac{M_f(t)}{M_{f\infty}} - 1 \right) - k_{fm} \left( \frac{M_f(t)}{M_{f\infty}} - \frac{M_m(t)}{M_{m\infty}} \right), \\ \frac{d}{dt} \frac{M_m(t)}{M_{m\infty}} &= -R_{1m} \left( \frac{M_m(t)}{M_{m\infty}} - 1 \right) - k_{mf} \left( \frac{M_m(t)}{M_{m\infty}} - \frac{M_f(t)}{M_{f\infty}} \right) \end{aligned} \quad [2]$$

The subscripts  $f$  and  $m$  refer to the free and macromolecular proton pools.  $M_f(t)$  and  $M_m(t)$  are the longitudinal magnetizations at time  $t$ , whose equilibrium values are  $M_{f\infty}$  and  $M_{m\infty}$ .  $R_{1f}$  and  $R_{1m}$  are the longitudinal relaxation rates of the free and macromolecular pools when there is no MT between them, and  $k_{fm}$  and  $k_{mf}$  are the rates of magnetization transfer between them. The pool size ratio ( $p_m/p_f$ ) is defined by  $k_{fm}/k_{mf}$ . The recovery of the magnetization of the free pool is described by a bi-exponential decay function when there are no RF pulses:

$$\frac{M_f(t)}{M_{f\infty}} = b_f^+ e^{-R_1^+ t} + b_f^- e^{-R_1^- t} + 1 \quad [3]$$

where

$$\begin{aligned} 2R_1^\pm &= R_{1f} + R_{1m} + k_{fm} + k_{mf} \pm \sqrt{(R_{1f} - R_{1m} + k_{fm} - k_{mf})^2 + 4k_{fm}k_{mf}} \\ b_f^\pm &= \pm \frac{\left[ \frac{M_f(0)}{M_{f\infty}} - 1 \right] (R_{1f} - R_1^\pm) + \left[ \frac{M_f(0)}{M_{f\infty}} - \frac{M_m(0)}{M_{m\infty}} \right] k_{fm}}{R_1^+ - R_1^-} \end{aligned} \quad [4]$$

where  $R_1^+$  and  $R_1^-$  are the fast and slow recovery rates, respectively. The magnetization of the macromolecular pool is described by a bi-exponential equation as well, by exchanging  $f$  and  $m$  subscripts in Eqs. [3] and [4].

Applying Eqs. [3] and [4] to each free evolution period gives the signal as function of the qMT parameters, allowing us to investigate the problem and fit the qMT parameters without taking the first-order approximations utilized previously (8-10). Specifically, both pools have zero  $z$ -magnetization at the end of the FSE train, their magnetization at the end of  $t_d$  is written as

$$\begin{aligned}\frac{M_f(t_d^-)}{M_{f\infty}} &= -\frac{R_{1f}-R_1^-}{R_1^+-R_1^-}e^{-R_1^+t_d} + \frac{R_{1f}-R_1^+}{R_1^+-R_1^-}e^{-R_1^-t_d} + 1, \\ \frac{M_m(t_d^-)}{M_{m\infty}} &= -\frac{R_{1m}-R_1^-}{R_1^+-R_1^-}e^{-R_1^+t_d} + \frac{R_{1m}-R_1^+}{R_1^+-R_1^-}e^{-R_1^-t_d} + 1\end{aligned}\quad [5]$$

The effect of the inversion pulse is,

$$\begin{aligned}\frac{M_f(t_d^+)}{M_{f\infty}} &= S_f \frac{M_f(t_d^-)}{M_{f\infty}} \\ \frac{M_m(t_d^+)}{M_{m\infty}} &= S_m \frac{M_m(t_d^-)}{M_{m\infty}}\end{aligned}\quad [6]$$

where  $S_f$  and  $S_m$  are the inversion coefficients of the free and macromolecular pools, and  $t_d^-$  and  $t_d^+$  are the time just before and after the inversion pulse, respectively.

The model discussed above contains seven parameters:  $R_{1f}$ ,  $R_{1m}$ ,  $p_m/p_f$ ,  $k_{mf}$  ( $k_{fm}$  is equal to  $k_{mf} \times p_m/p_f$ ),  $S_f$ ,  $S_m$ , and  $M_{f\infty}$ . Among these parameters, the signal dependencies on  $S_m$  and  $R_{1m}$  are weak, as shown below. The weak dependence on  $R_{1m}$  is also the case in the pulsed saturation sequence (3-5,21). In this work,  $R_{1m}$  is set to be equal to  $R_{1f}$  for data analysis. Previous results (10) calculated an  $S_m$  of  $0.83 \pm 0.07$  from numerical simulations, for a 1-ms hard inversion pulse on a solid pool with a Gaussian lineshape and a  $T_2$  between 10  $\mu$ s and 20  $\mu$ s. There are then five remaining qMT parameters to fit:  $R_{1f}$ ,  $p_m/p_f$ ,  $k_{mf}$ ,  $S_f$  and  $M_{f\infty}$ .  $S_f$  is expected to be  $-1$ , but due to  $B_0$  and  $B_1$  inhomogeneities, it has to be fit from experimental data. Finally, combining Eqns. [3-6] for each time period gives a signal function, which we use to fit the qMT parameters directly without first-order approximations.

### CRLB Theory

The optimization technique presented in this work is similar to that of Cercignani *et al.* (21), but is applied to a different pulse sequence and includes acquisition time effects when calculating parameter precisions. For a set of particular qMT parameters, the CRLB derived objective function is:

$$V = \left( \sum_{j=1}^Q [J^{-1}]_{jj} p_j^{-2} \right) \times T_{\text{cost}}(\text{scheme}) \quad [7]$$

where  $Q$  is the number of fitted parameters, and  $p_j$  is the  $j^{\text{th}}$  parameter.  $T_{\text{cost}}(\text{scheme})$  is given by:

$$T_{\text{cost}}(\text{scheme}) = \sum_{n=1}^N (t_{i,n} + t_{d,n} + t_{fse}) \quad [8]$$

where  $N$  is the number of sampling points,  $t_{fse}$  is the length of the FSE train, and  $t_{i,n}$  and  $t_{d,n}$  are the  $n$ th  $t_i$  and  $t_d$  values. The Fisher information matrix  $J$  is defined by its  $jk^{th}$  element

$$J_{jk} = \frac{1}{\sigma^2} \sum_{n=1}^N \left( \frac{\partial S(p_1, \dots, p_Q; x_n)}{\partial p_j} \frac{\partial S(p_1, \dots, p_Q; x_n)}{\partial p_k} \right) \quad [9]$$

where  $p_j$  is the  $j^{th}$  parameter,  $x$  are the  $(t_i, t_d)$  sampling points, and  $S$  are the signal function. The standard deviation (SD) of noise,  $\sigma$  is assumed to be independent of  $x$ . As pointed out in

(21), the essence of the term  $\sum_{j=1}^Q [J^{-1}]_{jj} p_j^{-2}$  in Eq. [7] is  $\sum \sigma_j^2 / p_j^2$  where  $\sigma_j^2$  is the variance of the parameter  $p_j$ . By including the time cost term in Eq. [7], the objective function becomes essentially the inverse of precision efficiency (precision-per-unit-time (27)). The optimization process yields the maximum precision efficiency, by searching for the minimum value of the objective function.

For optimization of heterogeneous samples, CRLB objective functions are constructed in a similar form as in (21):

$$V_{\max} = \max_l \left\{ \sum_{i=1}^Q [J_l^{-1}]_{ii} p_{il}^{-2} \right\} T_{\text{cost}} (\text{scheme}) \quad [10]$$

Where  $l$  indexes parameter sets that characterize different tissues. Minimizing  $V_{\max}$  by varying the sample points  $x$  would maximize the precision efficiency for the worst combination of parameters.

### Optimization Technique

The optimization process searches for the optimal acquisition schemes,  $x_1, \dots, x_N$  that minimize  $V$  and  $V_{\max}$  defined in Eqs. [7] and [10]. A simulated annealing algorithm (28) was implemented in Matlab 2008b (The Mathworks, Natick, MA, USA) to search for the optimal acquisition schemes. It evaluates 500 objective functions at each temperature  $T$  by randomly varying  $x_1, \dots, x_N$ , i.e., all  $t_i$  and  $t_d$  values. The objective function is randomly perturbed by using a Metropolis algorithm (29), which allows uphill transitions and increases the possibility of reaching a global minimum. The temperature decreases according to the annealing schedule

$$T(n+1) = T(n) \times (1 - \varepsilon) \quad [11]$$

where  $0 < \varepsilon \ll 1$ , until it reaches the final temperature. The initial and final temperatures are set as 100 and 0.001. To reduce the effects of local minima, the optimization is repeated from several random starting points. The scheme with a minimum objective function value is selected. The simulated annealing does not guarantee a global minimum, but we do not expect dramatic improvement in the objective function values.

By utilizing this technique, a series of optimization processes were performed. We optimized  $T_I$  precision efficiency (using Eqs. [1, 7-10]) by varying all  $t_i$  and a single  $t_d$  values, and by varying all  $t_i$  and  $t_d$  values. A set of typical parameters values are:  $M_f = 1$ ,  $T_I = 1$ , and  $S_f = -1$ . The optimization of parameter ranges are:  $M_0 \in [0.5, 1.5]$ ,  $T_I \in [0.5, 1.5]$ , and  $S_f \in [-0.85, -1]$ .

For qMT precision efficiency optimization, we searched for optimal acquisition schemes that have approximately the same total acquisition time as the original scheme given in (10), by repeating the optimization process while varying the number of sampling points and then selecting the scheme that most closely matches the total acquisition time of the original. A set of typical qMT parameters (roughly those of WM) are:  $R_{1f} = 0.5$  Hz,  $p_m/p_f = 0.10$ ,  $k_{mf} = 30$  Hz,  $S_f = -0.95$ , and  $M_{f\infty} = 1.0$ , with  $R_{1m} = 0.5$  Hz and  $S_m = 0.83$ .  $R_{1f}$  and  $R_{1m}$  values are smaller than the values presented in (9) because the measurements in this work are performed at higher magnetic field strengths.  $M_{f\infty}$  is simply set to 1.0 since it is only a scaling factor. The optimization of parameter ranges are:  $R_{1f} \in [0.4, 1.0]$ ,  $p_m/p_f \in [0.05, 0.20]$ ,  $k_{mf} \in [20, 40]$ ,  $S_f \in [-1.0, -0.9]$ , and  $M_{f\infty} \in [0.6, 1.5]$ . This process takes more time because it has to calculate 33 parameter combination sets ( $2^5 = 32$  combinations of the listed parameter values plus one set of midpoint values). The lower limit of  $t_i$  and  $t_d$  are set as 4 ms and 10 ms, respectively. These parameter ranges encompass those of the (WM) and GM (10), so the optimal schemes are directly applicable to *in vivo* brain measurements.

## Imaging methods

In the SIR-FSE sequence diagrammed in Figure 1, we applied 16 refocusing pulses with 10-ms spacing. We acquired data only during the first eight echoes, applying an additional eight pulses in order to ensure zero z-magnetization in both the free water and macromolecular pools at the end of the echo train. The initial inversion pulse is a 1-ms  $180^\circ$  hard pulse. The  $90^\circ$  and  $180^\circ$  refocusing pulses are 1-ms 5-lobe sinc pulses, with time bandwidth product (TBW) of 5.92 and 4.44, respectively. For each measurement, two dummy scans were applied and four or eight acquisitions were averaged, with phase cycling of the  $90^\circ$  and acquisition, but no cycling of the initial inversion pulse (in order to destroy residual transverse magnetization). Gradient spoilers were also applied after the inversion pulse.

$T_1$  measurements were made on a 9.4 T Varian system with a 38-mm litz coil.  $MnCl_2$  samples of 0.058 mM and 0.116 mM were prepared. Images were acquired with a FOV of  $28 \times 28$  mm<sup>2</sup>, slice thickness of 2 mm, and data matrix of  $32 \times 32$ . A conventional scheme, with a long  $t_d$  of 6 s, and ten logarithmic-spaced  $t_i$  values varied between 1 and 6 s, was applied, with four acquisitions averaged. In addition, eight optimized schemes were developed and applied. Four of the schemes were optimized for  $M_0 = 1$ ,  $T_1 = 1$  s, and  $S_f = -1$ , and four for the parameter ranges  $M_0 \in [0.5, 1.5]$ ,  $T_1 \in [0.5, 1.5]$ , and  $S_f \in [-0.85, -1]$ . Each set of four consisted of one optimization of  $t_i$  values with a single  $t_d$  of 1 s, and three optimizations where both  $t_i$  and  $t_d$  were allowed to vary amongst 10, 5, or 3 values. For ten-point optimal schemes, four acquisitions were averaged, while for five- and three-point schemes, eight acquisitions were averaged, to achieve roughly similar SNRs for a comparison.

A series of bovine serum albumin (BSA) samples served as test phantoms for the qMT measurements. The BSA samples have percent weights of 10, 15, 20, and 25, with corresponding BSA to water ratios of 0.11, 0.18, 0.25, and 0.33. An additional sample of 15% BSA with 0.05 mM  $MnCl_2$  was measured as well in order to separate MT from relaxation effects. All samples were cross-linked using 25% glutaraldehyde. Measurements on these BSA samples were performed on a 4.7 T Varian system with a 63-mm quad coil. Images were acquired with FOV of  $40 \times 40$  mm<sup>2</sup>, slice thickness of 2 mm, and data matrix of  $64 \times 64$ . Two sets of experiments were performed on the BSA phantom: 1) a comparison of a previous method (10) with two optimized methods with the same acquisition time (~1 hour), and 2) a comparison of two optimized methods with 5 and 10 sampling points (and eight or four averages) with the same 16 minute acquisition time. All schemes were optimized for sample parameters that roughly match white matter, but are also a fairly good match for BSA. A measurement of  $R_2$  was performed as well, by using a multiple spin echo imaging sequence (TR/TE = 15000/12 ms, 15 echoes, and 4 averages).

To demonstrate that the optimized schemes are applicable to brain tissues, *in vivo* rat brain measurements were acquired using a five-point scheme optimized for parameter ranges. The measurement was performed on a 7.0 T Varian animal system, with a 38-mm litz coil. The FOV was  $38 \times 38 \text{ mm}^2$ , with a slice thickness of 1 mm and matrix of  $128 \times 128$ . To increase SNR, eight acquisitions were averaged, giving a total time of around 32 minutes.

## Results

### Optimal Schemes for determining $T_1$

For a typical parameter set of  $M_0 = 1$ ,  $S_f = -1$ , and  $T_1 = 1$ , and a conventional acquisition scheme, which consists of a constant  $t_d$  of 6 s and a ten-point logarithmic spacing of  $t_i$  between 4 ms and  $t_d$  of 6 s. The objective function value of this scheme, calculated from Eqs. [1] and [7], is 286.1 s. A ten-point scheme, which optimizes for  $t_i$  and a single  $t_d$  (1s), has an objective function value of 62.4 s. The 1-s  $t_d$  value was found to be the optimal one by comparing objective function values of optimal schemes with different  $t_d$  values. Finally, for an optimal scheme with ten independently varied  $t_i$  and  $t_d$  values, the objective function value is 44.0 s. There is little variation in the objective function when there are 10 (44.0 s) or 3 (49.8 s)  $t_i$  and  $t_d$  values, we plot below a similar lack of dependence on sampling point numbers in the qMT optimization case, shown in Figure 2. Note that we have found that the minimum number of sampling points is three for  $T_1$  determinations, with a total acquisition time of about 11s for one shot.

### Optimal schemes for determining qMT parameters

Table 1 lists three different schemes that have roughly equal acquisition times: the original scheme (Column 1), the optimal scheme for typical qMT parameters (Column 2) and the optimal scheme for qMT parameter ranges (Column 3). For scheme (1), its objective function values are  $V = 3.14 \times 10^4 \text{ s}$  and  $V_{\max} = 7.82 \times 10^5 \text{ s}$ . For scheme (2), its objective function values are  $V = 1.39 \times 10^4 \text{ s}$  and  $V_{\max} = 3.35 \times 10^5 \text{ s}$ . For scheme (3), its objective function values are  $V = 1.51 \times 10^4 \text{ s}$  and  $V_{\max} = 3.25 \times 10^5 \text{ s}$ . Note that for scheme (2), the sampling points fall into seven groups, effectively making it a seven-point sequence with variation in the SNR of each point. As for the original scheme, the objective function does not reflect the additional errors that come from the first-order approximations previously employed (9,10).

### Investigation of number of sampling points for qMT measurements

As illustrated in scheme (2) in Table 1, we can determine qMT parameters with a much smaller number of sampling points. The optimization program was repeated while varying the number of sampling points, N. It is found that, for different N, the optimization processes yield similar objective function values, and only five sampling points are required to fit for five qMT parameters. In Figure 2, plots of calculated relative precision efficiencies vs. number of sampling points are shown, optimized for parameter ranges and the “typical” parameter set, respectively. Note that the precision efficiency is defined by the square root of the inverse of the CRLB objective function value, which is  $1/\sqrt{V}$ . The precision efficiency decreases only slightly (2% drop for the parameter ranges and 4% drop for the typical parameter set) at small N, meaning that there is little penalty in the fitted parameter precision efficiencies when minimizing the acquisition time by decreasing the number of acquired images, assuming one employs the optimum  $t_i$  and  $t_d$  values at each N.

### Monte Carlo Simulations

Monte Carlo simulations were performed at different noise levels to measure the uncertainties of fitted parameters for the optimal schemes. At each noise level, 10000 data

sets were generated. Gaussian noise was introduced at each SNR level. Each data set was then fitted. The mean and standard deviation of the fits define the schemes' systematic errors and uncertainties, respectively.

For  $T_I$  simulations, the selected parameters are  $M_0 = 1$ ,  $S_f = -1$ , and  $T_I = 1$ . Figure 3 shows a comparison between a conventional scheme, with ten-point logarithmic spacing of  $t_i$  between 4 ms and 6 s, and  $t_d$  of 6 s, and a three-point optimal scheme, with both  $t_i$  and  $t_d$  varied. Only  $T_I$  results are shown. The optimal scheme yields much less uncertainties in  $T_I$  values than the conventional one, with uncertainties normalized to same total acquisition time.

For qMT simulations, the selected parameters used to generate the data are  $R_{If} = 0.5$ ,  $p_m/p_f = 0.1$ ,  $k_{mf} = 30$ ,  $S_f = -0.95$ , and  $M_{f\infty} = 1$ . The comparison of scheme (1) and (2) is shown in Figure 4. Scheme (3) has similar performances as scheme (2), as reflected in their objective function values, and its simulation result is not shown.  $M_{f\infty}$  is not shown either because both schemes produce similar results. The simulation data of the original scheme (1) were processed both with and without first-order approximations. It is obvious that for the original scheme, this approximation causes systematic errors in the fitted  $p_m/p_f$ ,  $k_{mf}$  and  $S_f$  values, and that for  $k_{mf}$  and  $p_m/p_f$ , these errors have a fractional size on the order of the pool size ratio. Scheme (1) and (2) without approximations avoid these systematic errors. Scheme (2) also produces more precise values of  $p_m/p_f$ ,  $k_{mf}$  than scheme (1), especially at low SNR. Additional simulations not shown here indicate that for the worst combination of parameter set, scheme (3) yield the least uncertainties, as reflected in its  $V_{max}$  value.

## Measurements

The measured  $T_I$  values of  $MnCl_2$  samples by using different acquisition schemes are plotted in Figure 5. The determined values and uncertainties are calculated from mean and standard deviation from pixels in the region of interest.

Figure 6 shows corresponding plots of  $R_{If}$ ,  $p_m/p_f$ ,  $k_{mf}$ ,  $S_f$  and  $M_{f\infty}$ . To show the effect of the new data processing technique, first-order approximations were employed to analyze the data acquired using scheme (1). The data from each pixel was fitted and qMT parameter values and uncertainties were set to the mean and standard deviation of the pixels in the regions of interest. The SNR of these measurements was around 270.

The comparison of measurement results using the five-point and ten-point optimal schemes is shown in Figure 7. It shows that both schemes produce similar qMT parameters within error ranges. Similar results are obtained for the five-point and ten-point schemes optimized for parameter ranges as well.

The *in vivo* measurement results with the five-point scheme are show in Figure 8. The determined qMT parameters of WM and GM are listed in Table 2.

## Discussion

In this paper, we have shown how to optimize the SIR-FSE sequences for  $T_I$  and qMT imaging using CRLB methods. The original qMT technique, presented in (9,10), used fixed  $t_d$  and varied  $t_i$  only and employed first-order approximations for data fitting. According to Monte Carlo simulations, as shown in Figure 4, first-order approximations will introduce systematic errors to  $p_m/p_f$ ,  $k_{mf}$  and  $S_f$ . The  $p_m/p_f$  values, determined by the original technique will be lower than the true value, while  $k_{mf}$  will be larger. In the new method presented here, we varied both  $t_d$  and  $t_i$  and fitted the qMT parameters with minimal approximations. Both the precision and accuracy increase, as shown in simulations and experimental results.

$T_1$  measurement has also been optimized using the same approach. By varying  $t_i$  and  $t_d$  independently, global optimal acquisition schemes were obtained with precision efficiencies, which are much greater than previous inversion recovery methods. This optimization is confirmed by Monte Carlo simulations, as shown in Figure 3, by comparing a ten-point conventional scheme with a three-point optimal scheme with same total acquisition time. Figure 5 shows a comparison of measured  $T_1$  values between the conventional scheme and a series of optimal schemes. It is shown that the optimal schemes yield consistent  $T_1$  values across schemes, which validates the optimization technique. It is also verified that only three sampling points are required to determine  $T_1$  value, as shown in schemes (h) and (i) in Figure 5. The three-point scheme optimized for parameter ranges of  $M_0 \in [0.5, 1.5]$ ,  $T_1 \in [0.5, 1.5]$ , and  $S_f \in [-0.85, -1]$ , is given in Table 3, which requires about 11s per acquisition, so, depending on SNR requirements, an 8 shot clinical scan would take 11s/shot  $\times$  8 shots  $\times$  2 averages = 3 minutes (Two averages allow phase cycling that destroys any transverse magnetization remaining after the gradient spoiling; Using a single average and fewer shots will proportionally lower the acquisition time).

The qMT optimization results were confirmed by the experimental measurements of BSA samples, as shown in Figure 6. The optimal schemes have less uncertainty in the measured qMT parameters, most notably in  $k_{mf}$ , which, due to its greater fractional uncertainty tends to dominate the calculation in Eq. [7]. The performances of schemes (2) and (3) are similar, which is not surprising, given their similar V values in Table 1. Therefore, the optimal scheme for the set of typical parameters is applicable to a range of qMT parameters for BSA samples of different percent weights. In other words, if the qMT parameters do not cover a very wide range, we will be able to optimize for a single parameter inside this range and apply the optimized scheme for all measurements. In addition, as in (9), the  $R_{1f}$ ,  $p_m/p_f$  values increase linearly with the BSA-to-water ratios. Note that the results from two 15% BSA samples are plotted, both with and without  $MnCl_2$ . The  $MnCl_2$  changes  $R_{1f}$  and  $R_2$  while having little effect on the fitted MT parameters, confirming that SIR-FSE is a true qMT sequence, and not just a function of the relaxation rates.

To further confirm the optimization technique, experimental precision efficiencies were calculated. Examples are given for qMT schemes (1), (2) and (3), as listed in Table 1. The CRLB theory predicts precision efficiency ratios of 1: 1.5: 1.45, from their V values. Monte Carlo simulations lead to precision efficiency ratios of 1: 1.56: 1.50, by extracting the simulation data at an SNR of 200. The experimental precision efficiency ratios of the qMT parameters of the 15% BSA are 1: 1.69: 1.35. These roughly similar ratios illustrate the advantage of the optimization technique. Consistent precision efficiency ratios were obtained for  $MnCl_2$  samples  $T_1$  measurements as well. A detailed comparison of relative precision efficiencies, derived from CRLB, Monte Carlo simulations and experimental results of  $T_1$  and qMT results is given in Figure 9. The experimental precision efficiencies were calculated from the 0.058 mM  $MnCl_2$  and 15% BSA samples, respectively. By varying  $t_i$  and  $t_d$  simultaneously, the precision efficiencies of  $T_1$  and qMT measurements has increased roughly 150% and 50%, respectively, comparing with the conventional scheme and original technique.

Figure 2 shows that the precision efficiency has only a weak dependence on the number of acquisitions, N. This indicates that we can take as few as five sampling points to determine the qMT parameters. This conclusion is confirmed by measurement of the BSA samples with five-point and ten-point schemes, as shown in Figure 7. It is further confirmed by *in vivo* measurements using the five-point scheme, as shown in Figure 8. The extracted qMT parameters of WM and GM are shown in Table 2. As shown in Monte Carlo simulations, the fitting process with first-order approximations leads to slightly larger  $k_{mf}$  but lower  $p_m/p_f$

values. This prediction is consistent with the differences between the qMT parameter values for WM in Table 2 and those in (10).

With the verification that only a five-point scheme is required to determine the five qMT parameters, this work provides more insight in rapid qMT acquisitions. For example, a five-point optimal scheme requires about 15s/acquisition, so, depending on SNR requirements, an 8 shot clinical scan would take 15s/shot  $\times$  8 shots  $\times$  2 averages = 4 minutes, making clinical application a possibility. A five-point scheme, proposed in this work for clinical applications, is shown in Table 4, which is optimized for above-mentioned parameter ranges.

A related issue for clinical application is the robustness of the standard FSE implementation on a given imaging system. Any ghosting or  $T_2$  blurring will cause correlating effects in the SIR-FSE qMT imaging sequence. Also, given the significant MT effects from the off-resonance excitation and refocusing pulses (30,31), multi-slice acquisitions do not make sense for SIR-FSE. However, 3D acquisitions are viable, at least in a research setting, e.g. a  $128 \times 128 \times 32$  3D volume could be acquired in 2 averages  $\times$  15s / excitation  $\times$  128  $\times$  32 phase encodes / 64 echoes = 32 minutes, not including benefits from partial k-space and parallel imaging effects. This acquisition time is comparable to pulsed saturation methods (32), but without the need for separate  $B_1$ ,  $B_0$ , and  $T_1$  maps. Pulsed saturation has, however, been more extensively tested *in vivo*.

In this work, we have given equal weights to all fitted parameter uncertainties in Eqs. [7] and [10]. Among the five qMT parameters, the pool size ratio ( $p_m/p_f$ ) is often of most interest. An alternative would be to optimize for  $p_m/p_f$  only. Optimization results, which are not shown, indicate an increase in  $p_m/p_f$  precision about 30% from such optimization, but at the cost of large systematic errors in the other qMT parameters, making it an unappealing alternative.

Fitting qMT parameters necessitates assumption about  $R_{Im}$  and  $S_m$ . We performed Monte Carlo simulations to investigate the variances of fitted qMT parameters vs. different underlying  $R_{Im}$  and  $S_m$  values. We found that the fitted  $R_{If}$ ,  $k_{mf}$ ,  $S_f$ , and  $M_{f\infty}$  values are almost independent of  $R_{Im}$  and  $S_m$ . The pool size ratios,  $p_m/p_f$ , has little dependence on  $R_{Im}$  but a relatively large dependence on  $S_m$ . The simulated data were generated with  $R_{If} = 0.5$ ,  $p_m/p_f = 0.1$ ,  $k_{mf} = 30$ ,  $S_f = -0.95$ , and  $M_{f\infty} = 1$ , by using scheme (2) in Table 1 at SNR of 100. For  $S_m = 0.76$  and  $0.9$ , the fitted  $p_m/p_f$  values are  $0.104 \pm 0.005$  and  $0.096 \pm 0.005$ , respectively. With these variations, the maximum uncertainty of  $p_m/p_f$  is about 10%, which indicates that this technique is fairly robust to assumptions of  $R_{Im}$  and  $S_m$ .

## Conclusion

In conclusion, we have shown how to optimize the SIR-FSE sequences by maximizing the precision efficiency using an objective function, which includes CRLB and time cost. By varying both  $t_i$  and  $t_d$ , the precision efficiencies of both  $T_1$  and qMT measurements are increased. Monte Carlo simulations support this approach by showing reduction in the uncertainties of fitted parameters. The optimization results are confirmed by measurements on  $MnCl_2$  samples, BSA samples, and *in vivo* rat brain. Specifically, for qMT determinations, minimal approximations were applied to get rid of the systematic errors from first-order approximations in previous work (8-10). From the investigation of number of sampling data points, it is shown that five data points are enough to determine qMT parameters, and three data points are enough to determine  $T_1$  parameters. This opens up the possibility of applying the SIR-FSE sequences to clinical 2D and preclinical 3D applications.

## Acknowledgments

Grant sponsor: NIH EB001452, EB00214, EB001744 and NFS 0448915. The authors thank Dr. Heather Whitney for assistance in BSA phantom preparation.

Grant Sponsor: NIH EB001452, EB00214, EB001744 and NFS 0448915

## References

1. Wolff SD, Balaban RS. Magnetization Transfer Contrast (Mtc) and Tissue Water Proton Relaxation In Vivo. *Magn Reson Med.* 1989; 10(1):135–144. [PubMed: 2547135]
2. Henkelman RM, Huang XM, Xiang QS, Stanisz GJ, Swanson SD, Bronskill MJ. Quantitative Interpretation of Magnetization-Transfer. *Magn Reson Med.* 1993; 29(6):759–766. [PubMed: 8350718]
3. Sled JG, Pike GB. Quantitative interpretation of magnetization transfer in spoiled gradient echo MRI sequences. *J Magn Reson.* 2000; 145(1):24–36. [PubMed: 10873494]
4. Sled JG, Pike GB. Quantitative imaging of magnetization transfer exchange and relaxation properties in vivo using MRI. *Magn Reson Med.* 2001; 46(5):923–931. [PubMed: 11675644]
5. Ramani A, Dalton C, Miller DH, Tofts PS, Barker GJ. Precise estimate of fundamental in-vivo MT parameters in human brain in clinically feasible times. *Magn Reson Imaging.* 2002; 20(10):721–731. [PubMed: 12591568]
6. Gloor M, Scheffler K, Bieri O. Quantitative magnetization transfer imaging using balanced SSFP. *Magn Reson Med.* 2008; 60(3):691–700. [PubMed: 18727085]
7. Ropele S, Seifert T, Enzinger C, Fazekas F. Method for quantitative imaging of the macromolecular 1H fraction in tissues. *Magn Reson Med.* 2003; 49(5):864–871. [PubMed: 12704769]
8. Gochberg DF, Kennan RP, Gore JC. Quantitative studies of magnetization transfer by selective excitation and T-1 recovery. *Magn Reson Med.* 1997; 38(2):224–231. [PubMed: 9256101]
9. Gochberg DF, Gore JC. Quantitative imaging of magnetization transfer using an inversion recovery sequence. *Magn Reson Med.* 2003; 49(3):501–505. [PubMed: 12594753]
10. Gochberg DF, Gore JC. Quantitative magnetization transfer imaging via selective inversion recovery with short repetition times. *Magn Reson Med.* 2007; 57(2):437–441. [PubMed: 17260381]
11. Edzes HT, Samulski ET. The measurement of cross-relaxation effects in the proton NMR spin-lattice relaxation of water in biological systems: Hydrated collagen and muscle. *Journal of Magnetic Resonance.* 1978; 31(2):207–229. 1969.
12. Edzes HT, Samulski ET. Cross relaxation and spin diffusion in the proton NMR of hydrated collagen. *Nature.* 1977; 265(5594):521–523. [PubMed: 834303]
13. Morris GA, Freemont AJ. Direct observation of the magnetization exchange dynamics responsible for magnetization transfer contrast in human cartilage in vitro. *Magn Reson Med.* 1992; 28(1):97–104. [PubMed: 1435226]
14. Sobol WT, Pintar MM. NMR spectroscopy of heterogeneous solid-liquid mixtures. Spin grouping and exchange analysis of proton spin relaxation in a tissue. *Magn Reson Med.* 1987; 4(6):537–554. [PubMed: 3613954]
15. Prantner AM, Bretthorst GL, Neil JJ, Garbow JR, Ackerman JJ. Magnetization transfer induced biexponential longitudinal relaxation. *Magn Reson Med.* 2008; 60(3):555–563. [PubMed: 18759367]
16. Kay, SM. *Fundamentals of Statistical Signal Processing.* Prentice-Hall; 1993.
17. Ogg RJ, Kingsley PB. Optimized precision of inversion-recovery T-1 measurements for constrained scan time. *Magn Reson Med.* 2004; 51(3):625–630. [PubMed: 15004808]
18. Jones JA, Hodgkinson P, Barker AL, Hore PJ. Optimal sampling strategies for the measurement of spin-spin relaxation times. *J Magn Reson Series B.* 1996; 113(1):25–34.
19. Brihuega-Moreno O, Heese FP, Hall LD. Optimization of diffusion measurements using Cramer-Rao lower bound theory and its application to articular cartilage. *Magn Reson Med.* 2003; 50(5):1069–1076. [PubMed: 14587018]

20. Dula AN, Gochberg DF, Does MD. Optimal echo spacing for multi-echo imaging measurements of Bi-exponential T-2 relaxation. *J Magn Reson.* 2009; 196(2):149–156. [PubMed: 19028432]
21. Cercignani M, Alexander DC. Optimal acquisition schemes for in vivo quantitative magnetization transfer MRI. *Magn Reson Med.* 2006; 56(4):803–810. [PubMed: 16902982]
22. Crawley AP, Henkelman RM. A comparison of one-shot and recovery methods in T1 imaging. *Magn Reson Med.* 1988; 7(1):23–34. [PubMed: 3386519]
23. Look DC, Locker DR. Time Saving in Measurement of NMR and EPR Relaxation Times. *Review of Scientific Instruments.* 1970; 41(2):250–251.
24. Wang HZ, Riederer SJ, Lee JN. Optimizing the precision in T1 relaxation estimation using limited flip angles. *Magn Reson Med.* 1987; 5(5):399–416. [PubMed: 3431401]
25. Christensen KA, Grant DM, Schulman EM, Walling C. Optimal Determination of Relaxation-Times of Fourier-Transform Nuclear Magnetic-Resonance - Determination of Spin-Lattice Relaxation-Times in Chemically Polarized Species. *Journal of Physical Chemistry.* 1974; 78(19):1971–1977.
26. Wang J, Qiu M, Kim H, Constable RT. T1 Measurements incorporating flip angle calibration and correction in vivo. *J Magn Reson.* 2006; 182(2):283–292. [PubMed: 16875852]
27. Fleysher L, Fleysher R, Liu ST, Zaaraoui W, Gonen O. Optimizing the precision-per-unit-time of quantitative MR metrics: Examples for T-1, T-2, and DTI. *Magn Reson Med.* 2007; 57(2):380–387. [PubMed: 17260375]
28. Kirkpatrick S, Gelatt CD, Vecchi MP. Optimization by Simulated Annealing. *Science.* 1983; 220(4598):671–680. [PubMed: 17813860]
29. Metropolis N, Rosenbluth AW, Rosenbluth MN, Tell AH. Equation of State Calculations by Fast Computing Machines. *J Chem Phys.* 1953; 21:1087.
30. Melki PS, Mulkern RV. Magnetization transfer effects in multislice RARE sequences. *Magn Reson Med.* 1992; 24(1):189–195. [PubMed: 1556927]
31. Dixon WT, Engels H, Castillo M, Sardashti M. Incidental magnetization transfer contrast in standard multislice imaging. *Magn Reson Imaging.* 1990; 8(4):417–422. [PubMed: 2392030]
32. Cercignani M, Symms MR, Schmierer K, Boulby PA, Tozer DJ, Ron M, Tofts PS, Barker GJ. Three-dimensional quantitative magnetisation transfer imaging of the human brain. *Neuroimage.* 2005; 27(2):436–441. [PubMed: 15978842]

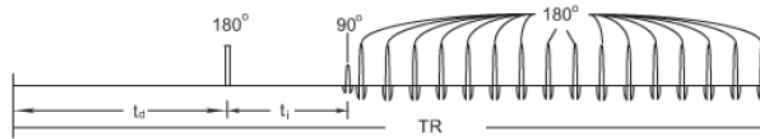


**Figure 1.** The SIR-FSE pulse sequence. The quantity  $t_d$  is the pre-delay time and  $t_i$  is the inversion recovery time. In this work, the first eight echoes are taken for data acquisition, and the next eight echoes were taken as dummy echoes to ensure the assumption of zero  $M_z$  magnetization of both pools after the last  $180^\circ$  pulse. A simulation of this sequence is presented in Ref. (10).

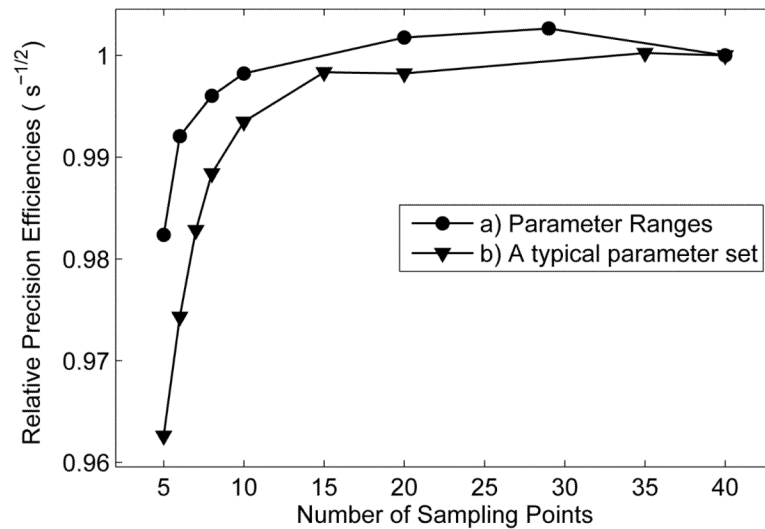


**Figure 2.**

Plots of relative precision efficiencies vs. sampling numbers after optimizing the acquisition parameters  $t_i$  and  $t_d$ . a) Optimizing for parameter ranges of:  $R_{1f} \in [0.4, 1.0]$  Hz,  $p_m/p_f \in [0.05, 0.20]$ ,  $k_{mf} \in [20, 40]$  Hz,  $S_f \in [-1.0, -0.9]$ , and  $M_{f\infty} \in [0.6, 1.5]$ , with precision efficiency defined by  $1/\sqrt{V_{\max}}$ . b) Optimizing for a single typical parameter set:  $R_{1f} = 0.5$  Hz,  $p_m/p_f = 0.10$ ,  $k_{mf} = 30$  Hz,  $S_f = -0.95$ , and  $M_{f\infty} = 1.0$ , with precision efficiency defined by  $1/\sqrt{V}$ . The efficiencies are normalized to the last data point in the two curves, respectively.

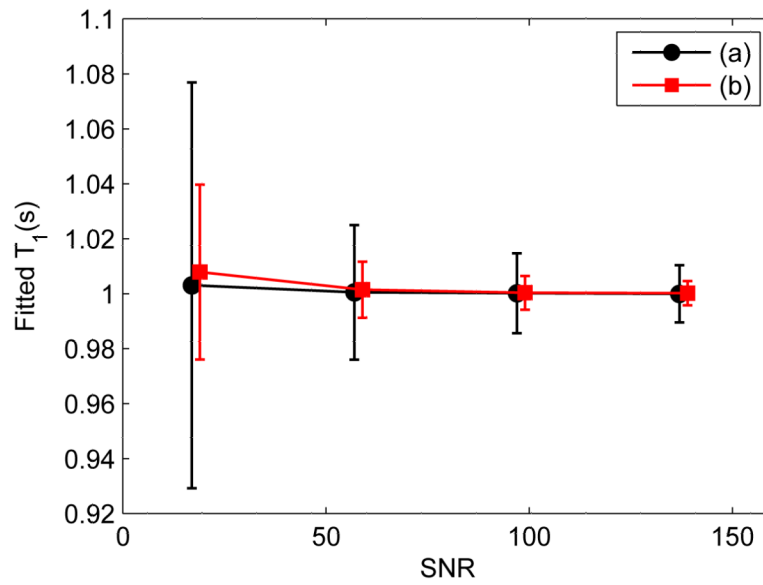


**Figure 3.** Monte Carlo simulation of  $T_1$  fitting results vs. SNR using schemes: (a) a ten-point conventional scheme (black) with  $t_1$  logarithmically varied between 4 ms and 6 s, and  $t_d$  of 6 s; (b) a three-point scheme (red) optimized for parameter values of  $M_0 = 1$ ,  $T_1 = 1$  s, and  $S_f = -1$ . Data points are slightly shifted to allow a clear comparison. The uncertainties are normalized for same total acquisition time.

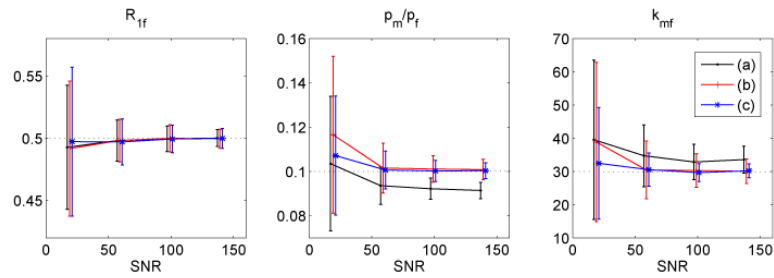


**Figure 4.** Monte Carlo Simulation of qMT fitting results vs. SNR: (a) scheme (1) (black) with first-order approximations, (b) scheme (1) (red) with direct fitting, and (c) scheme (2) (blue) with direct fitting. True values are indicated by dot lines. Data points are slightly shifted to allow a clear comparison. Note that the previously employed first-order approximations in scheme (1) lead to systematic deviations from the input value, and that scheme (2) has significantly smaller  $k_{mf}$  uncertainties than scheme (1), even when no first-order approximations are made.

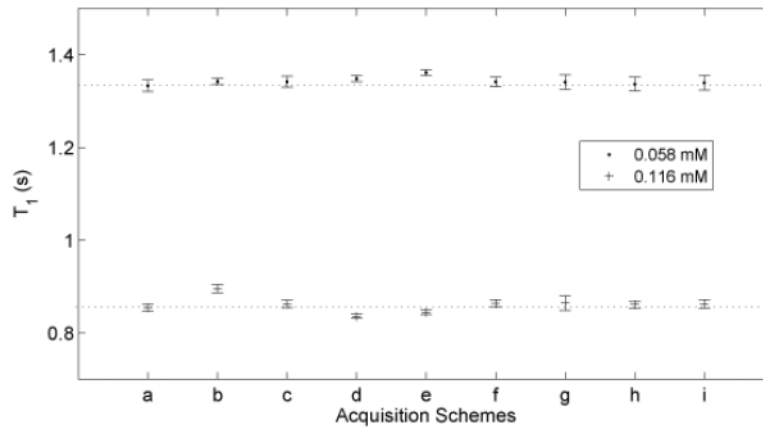


**Figure 5.**

Measured  $T_1$  values of  $\text{MnCl}_2$  samples of 0.058 mM and 0.116 mM by using several different acquisition schemes. (a) a ten-point conventional scheme with  $t_i$  logarithmically varied between 4 ms and 6 s, and  $t_d$  of 6 s. Schemes (b) and (c) are optimized by varying  $t_i$  values with a constant optimal  $t_d$  of 1s. Scheme (b) is optimized for parameter values of  $M_0 = 1$ ,  $T_1 = 1$ , and  $S_f = -1$ . Scheme (c) is optimized for parameter range values of  $M_0 \in [0.5, 1.5]$ ,  $T_1 \in [0.5, 1.5]$ , and  $S_f \in [-0.85, -1]$ . Schemes (d – i) are optimized by varying both  $t_i$  and  $t_d$  values. Schemes (d) (f) (h) are optimized for a single parameter set, as in (b), with numbers of sampling points of 10, 5, and 3, respectively. Schemes (e) (h) (i) are optimized for parameter range values as in (c), with numbers of sampling points of 10, 5, and 3, respectively. The determined values and uncertainties are calculated from the mean and standard deviation of the pixels in the region of interest.

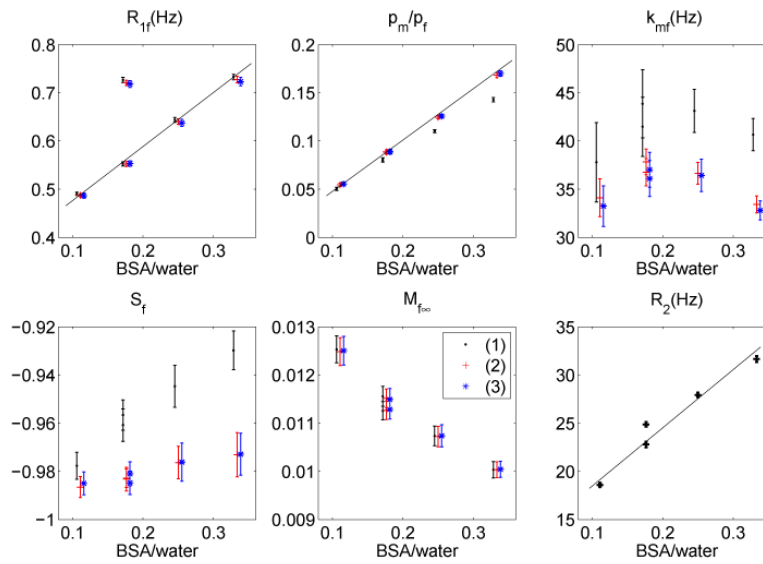


**Figure 6.**

Measured  $R_{1f}$ ,  $p_m/p_f$ ,  $k_{mf}$ ,  $S_f$ ,  $M_{f\infty}$  and  $R_2$  as a function of BSA weight vs. water weight ratio using acquisition schemes (1) (black), (2) (red) and (3) (blue), where  $M_{f\infty}$  is plotted in arbitrary units. Data points are shifted for a clear comparison. For scheme (1), first-order approximations were employed to process data. Note that the results from two 15% BSA samples are plotted, both with and without  $MnCl_2$ . The  $MnCl_2$  changes  $R_{1f}$  and  $R_2$  while having little effect on the fitted MT parameters, confirming that SIR-FSE is a true qMT sequence, and not just a function of the relaxation rates.

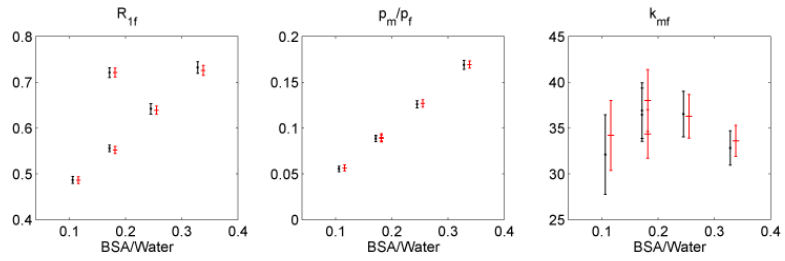


**Figure 7.**

A comparison of results measuring the BSA samples by employing a five-point scheme (black) and a ten-point scheme (red) with roughly the same acquisition time. Data points are shifted for a clear comparison. While the 10 point scheme has slightly smaller parameter uncertainties, as expected from Figure 2, there are no systematic differences in the results using the two schemes, except that the five-point scheme yielded higher  $M_f$  values due to more averages (not shown).

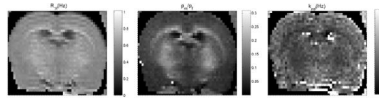


**Figure 8.**

Measured qMT parameter maps of a live rat with a five-point scheme, optimized for qMT parameter ranges. Images were acquired with a FOV of  $38 \times 38 \text{ mm}^2$  and slice thickness of 1 mm. Eight acquisitions were taken for data fitting. Note the elevated pool size ratio values due to myelin in the corpus callosum, as expected.

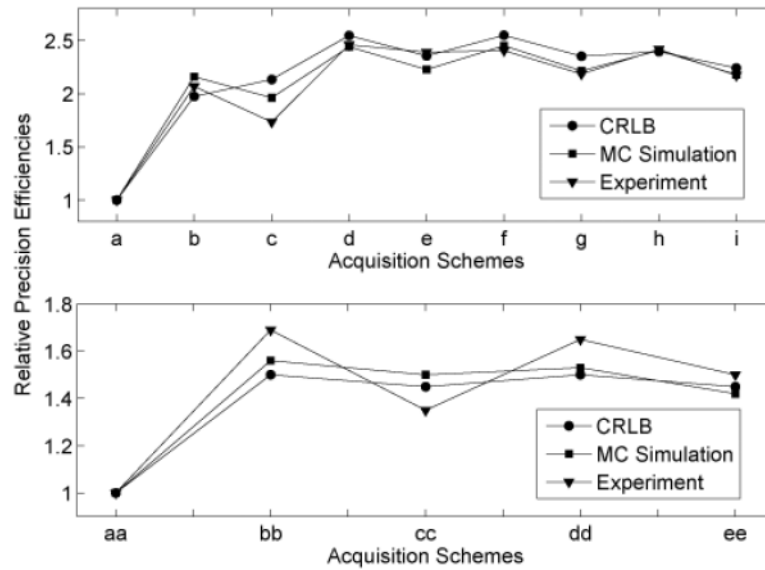


**Figure 9.**

Plot of relative precision efficiencies of  $T_1$  schemes and qMT schemes for the typical parameter values listed in Figure 2 and Figure 3. Schemes a-i are  $T_1$  schemes, as given in Figure 5. Schemes aa, bb, and cc are schemes (1)-(3) in Table 1. Schemes dd and ee are the ten- and five-point schemes in Figure 7. As shown in these plots, we have obtained: (1) an increase in the  $T_1$  precision efficiencies when optimizing both  $t_i$  and  $t_d$  of roughly 250% over logarithmic spacing and 25% over optimizing  $t_i$  and only a single  $t_d$ ; 2) an increase in the qMT precision efficiency when optimizing both  $t_i$  and  $t_d$  of roughly 50% over the previous logarithmic spacing; 3) only a small decrease in the precision efficiency when lowering the number of sampling points.

**Table 1**

Original and optimal schemes with roughly the same total acquisition time

<b>1) Original Scheme(10):</b> $V = 3.14 \times 10^4$ s, $V_{\max} = 7.82 \times 10^5$ s, Time cost= 105.54 s.	<b>2) Optimized for a typical parameter set:</b> $V = 1.39 \times 10^4$ s, $V_{\max} = 3.35 \times 10^5$ s, Time cost = 105.55 s.	<b>3) Optimized for parameter ranges:</b> $V = 1.51 \times 10^4$ s, $V_{\max} = 3.25 \times 10^5$ s, Time cost= 103.25s.
$t_i$ (s) $t_d$ (s)	$t_i$ (s) $t_d$ (s)	$t_i$ (s) $t_d$ (s)
0.004 3.5	0.004 1.669	0.004 2.465
0.005 3.5	0.004 1.692	0.004 2.654
0.006 3.5	0.004 1.694	0.004 2.981
0.007 3.5	0.004 1.727	0.004 4.665
0.008 3.5	0.004 1.745	0.004 4.676
0.009 3.5	0.004 4.797	0.004 4.862
0.011 3.5	0.004 4.888	0.029 4.713
0.013 3.5	0.004 4.894	0.032 3.699
0.016 3.5	0.031 4.368	0.032 4.550
0.019 3.5	0.032 2.102	0.033 4.881
0.023 3.5	0.032 4.130	0.034 5.087
0.028 3.5	0.032 4.160	0.035 3.171
0.033 3.5	0.032 4.175	0.035 3.771
0.040 3.5	0.032 4.188	0.035 3.800
0.049 3.5	0.032 4.251	0.035 3.803
0.059 3.5	0.033 2.147	0.039 2.401
0.072 3.5	0.033 2.150	0.040 1.775
0.085 3.5	0.033 2.164	0.077 1.030
0.103 3.5	0.033 2.240	0.213 2.503
0.124 3.5	0.033 2.258	0.227 2.772
0.150 3.5	0.034 2.148	0.231 2.931
0.300 3.5	0.189 2.396	0.234 3.102
1.000 3.5	0.190 2.381	0.236 2.943
2.000 3.5	0.190 2.384	0.240 3.133
10.000 3.5	0.190 2.392	0.240 3.212
	0.190 2.428	0.240 3.292
	0.191 2.362	0.252 3.271
	0.191 2.388	1.514 0.010
	0.191 2.410	2.489 0.010
	0.191 2.443	
	0.192 2.436	
	0.193 2.437	
	0.194 2.383	
	1.635 0.010	

<b>1) Original Scheme(10):</b> $V = 3.14 \times 10^4$ s, $V_{\max} = 7.82 \times 10^5$ s, Time cost= 105.54 s.	<b>2) Optimized for a typical parameter set:</b> $V = 1.39 \times 10^4$ s, $V_{\max} = 3.35 \times 10^5$ s, Time cost = 105.55 s.	<b>3) Optimized for parameter ranges:</b> $V = 1.51 \times 10^4$ s, $V_{\max} = 3.25 \times 10^5$ s, Time cost= 103.25s.
$t_i$ (s) $t_d$ (s)	$t_i$ (s) $t_d$ (s)	$t_i$ (s) $t_d$ (s)
	3.296 0.011	

**Table 2**

Measured qMT parameters of WM and GM in a live rat brain

	$R_{1f}$ (Hz)	$P_m/P_f$	$k_{mf}$ (Hz)
WM	$0.677 \pm 0.076$	$0.173 \pm 0.023$	$13.1 \pm 2.9$
GM	$0.550 \pm 0.046$	$0.080 \pm 0.008$	$20.8 \pm 6.5$

**Table 3**

An optimized three-point scheme for parameter ranges of  $M_0 \in [0.5, 1.5]$ ,  $T_1 \in [0.5, 1.5]$  s, and  $S_f \in [-0.85, -1]$

$t_i$ (s)	0.004	0.898	4.781
$t_d$ (s)	1.480	3.454	0.010

**Table 4**

An optimized five-point scheme proposed for clinical applications, for qMT parameters in ranges of:  $R_{1f} \in [0.4, 1.0]$  Hz,  $p_m/p_f \in [0.05, 0.20]$ ,  $k_{mf} \in [20, 40]$  Hz,  $S_f \in [-1.0, -0.90]$ , and  $M_{f00} \in [0.6, 1.5]$

$t_1$ (s)	0.004	0.032	0.035	0.225	0.770
$t_4$ (s)	3.502	4.603	1.507	3.273	0.011